Open Ceramics 5 (2021) 100041

Contents lists available at ScienceDirect

Open Ceramics

journal homepage: www.editorialmanager.com/oceram

Properties of alkali-activated mortars with salt aggregate for sealing structures in evaporite rock

Patrick Sturm [a,*], Janis Moye [a,b], Gregor J.G. Gluth [a], Nico Vogler [a], Alexander Taffe [b], Hans-Carsten Kühne [a]

[a] Bundesanstalt für Materialforschung und -prüfung (BAM), Division 7.4 Technology of Construction Materials, Unter den Eichen 87, 12205 Berlin, Germany
[b] Hochschule für Technik und Wirtschaft Berlin, Fachgebiet Baustoffkunde, Bauwerksdiagnose und Zerstörungsfreie Prüfung, Wilhelminenhofstr. 75A, 12459 Berlin, Germany

ARTICLE INFO

Keywords:
Alkali-activated mortars
Heat of reaction
Sealing structures

ABSTRACT

Concrete structures for sealing of tunnels in the host rock are an essential part of systems for nuclear waste storage. However, concretes based on blended cements or magnesium oxychloride cements, which are commonly considered for this application, can deteriorate severely due to a significant heat of hydration and associated deformation and cracking. Alkali-activated materials (AAMs) offer a potential solution to this problem because of their low heat release during hardening. To explore their suitability for the construction of sealing structures in evaporite rock, various AAMs with salt aggregate were studied regarding fresh properties, heat release, mechanical properties and microstructure. The heat of reaction of the AAMs was up to 55% lower than that of a blended cement designed for sealing structures, indicating significant benefits for the intended application. Other relevant properties such as mechanical strength and permeability depended strongly on the mix-design of the AAMs and curing conditions.

1. Introduction

The main function of sealing structures for nuclear waste repositories is the compensation of local disaggregation and excavation damage of the host rock in order to assure the integrity of the geological barrier. The long-term sealing function of a barrier is mainly determined by stress-strain interactions between the host rock and the sealing structure, especially at early ages after construction, as well as the permeability with respect to gases and liquids at later ages. In Germany, the salt-containing 'Zechstein' formations are considered to be suitable as host rock for nuclear waste repositories, due to their low permeability. The storage of nuclear waste in evaporite rock, mainly consisting of rock salt, is therefore a research topic since the start of the first long-term experiments in the 1960s at the Asse site and the 1970s at the Morsleben site [1].

Currently, concretes based on blended Portland cements with a high proportion of supplementary cementitious materials (SCMs) as well as concretes based on magnesium oxychloride cement (MOC) are considered for the construction of sealing structures [2–7]. The former are advantageous because of their comparatively low heat of hydration and – particularly for applications in clay-based host rocks – because of the comparatively low pH of their pore solution [8–10]. Binders with a high proportion of SCMs can provide a high durability in contact with saturated NaCl solutions, but in contact with $MgCl_2$ solutions corrosion may occur [11].

MOC-based concretes are particularly suited to MgO-rich host rocks because of a similar, *i.e.* MgO-rich, composition and, thus, expected high compatibility and durability [3–5,12]. On the other hand, MOC-based concretes are not fully stable in contact with saturated NaCl-solutions and, due to the high solubility of the binder under standard conditions, its use in other applications is limited [11]. In addition, MOCs generally exhibit a very high heat of reaction [13].

Despite the significant progress that has been made regarding concretes based on SCM-rich binders and MOCs, problems still exist, particularly with cracking of sealing structures, presumably related to shrinkage and heat evolution during early hydration [6,13]. This crack formation can drastically increase the permeability of the structures, making them unsuitable for the intended application. This warrants exploration of other types of binders, that can be formulated to exhibit a considerably lower heat of reaction to minimize the formation of cracks caused by differential thermal deformations.

* Corresponding author.
E-mail address: patrick.sturm@bam.de (P. Sturm).

https://doi.org/10.1016/j.oceram.2020.100041
Received 6 October 2020; Received in revised form 24 November 2020; Accepted 2 December 2020
Available online 7 December 2020
2666-5395/© 2020 The Author(s). Published by Elsevier Ltd on behalf of European Ceramic Society. This is an open access article under the CC BY-NC-ND license (http://creativecommons.org/licenses/by-nc-nd/4.0/).

Alkali-activated materials (AAMs) are cementitious materials that can be synthesized by the activation of aluminosilicates, e.g. metakaolin (MK) or fly ash (FA), with alkaline activator solutions, such as alkali hydroxide or alkali silicate solutions (e.g. Ref. [14]). For so-called 'one-part' alkali-activated materials (OP AAMs), the handling of alkaline solutions is avoided by providing the activator in solid form in the dry binder [15]. Depending on the mix-design, the heat of reaction of AAMs [16,17] can be much lower than that of MOCs [13] and blended Portland cements [10], thus potentially providing significant benefits when employed for concrete sealing structures. The drying shrinkage of AAMs depends strongly on the employed feedstocks and the curing conditions [18,19]; very low drying shrinkage was observed for OP AAMs after initial curing at elevated temperature [20]. Besides heat evolution and shrinkage, other important properties of binders for sealing structures include mechanical properties and permeability; these vary widely between different AAMs, depending on their mix-design and curing conditions.

To investigate parameters that determine the suitability of AAMs for sealing structures in evaporite rock, AAM-based mortars with salt aggregate were tested and analyzed in the present study with regard to fresh mortar properties, heat of reaction, strength development, air permeability and microstructure. The mortars were compared to the blended Portland cement-based reference concrete 'M2-Salzbeton' (M2), which was developed for the nuclear waste repository 'Endlager für radioaktive Abfälle Morsleben' (ERAM) in Central Germany [2].

2. Raw materials and mortar production

2.1. Raw materials

Hard coal fly ash (FA) was used as the solid binder for the alkali-activated fly ash (AAFA) and as SCM for the blended M2 reference. The cement used for this reference was a ground granulated blast furnace slag-containing CEM III/B 32.5 N-LH/SR/NA. Silica fume (SF) and solid sodium aluminate (SA) were used as raw materials for the OP AAMs. The SA had an Al/Na ratio of 1.07 mol/mol; larger agglomerates in the SA were removed by sieving (mesh widths = 2 mm) before use.

For the employed FA, 80 ± 10% of the particles were smaller than 45 μm, and <10% were smaller than 1 μm, as determined by laser granulometry after dispersion in propan-2-ol. The size of the primary particles of the SF was in the range 100–200 nm, as seen in scanning electron micrographs [21].

Rock salt from a deposit of the 'Kaliwerk Zielitz' in Sachsen-Anhalt (Germany) was used as aggregate. Based on the measured Na_2O content (45.5 wt.-%, Table 1), the theoretical amount of NaCl was calculated to be ~91 wt% (dry salt). The actual NaCl content was slightly lower, because minor amounts of sodium and chloride were bound in the rock salt impurities as identified by XRD (not shown). Besides halite, the rock salt contained sylvite and chloromagnesite as well as low amounts of the sulfates anhydrite, mirabilite, arcanite, syngenite, polyhalite and langbeinite.

The chemical compositions of the solid raw materials, as determined by inductively coupled plasma optic emission spectroscopy (ICP-OES) after total microwave digestion, are shown in Table 1. The sodium silicate (SS) solution used for the AAFA had a composition of 14.6–15.4 wt% Na_2O + 26.7–27.8 wt% SiO_2; balance H_2O (manufacturer's data). The sodium hydroxide solution was prepared by mixing analytical-grade sodium hydroxide pellets and deionized water; its composition was 41.7 wt % NaOH +58.3 wt% H_2O.

2.2. Mortar production

The formulations of the OP AAM mortars are based on a filed German patent application [22]. The mix designs of all mortars are given in Table 2. The OP AAM mortars were prepared at nominal *w/b* ratios of 0.50 (O1 and O2) or 0.40 (O3). In some of the O1 mortars, 11.15 kg/m^3 of SA were exchanged with Na_2CO_3 (analytical grade); these samples are marked as O1_n below.

Table 1
Chemical compositions of the solid feedstocks.

Oxide	SF	SA	FA	CEM III/B	CEM I	Salt
	mass fraction (wt%)					
SiO_2	94.10	0.01	53.01	25.00	19.49	1.68
Al_2O_3	0.22	58.93	23.25	6.22	4.66	0.03
Fe_2O_3	0.08	0.02	7.77	1.46	2.82	0.02
TiO_2	0.01	0.01	0.68	0.53	0.15	<0.01
CaO	1.52	0.09	7.48	55.54	62.88	0.48
MgO	0.23	0.02	2.25	4.33	2.00	0.30
Na_2O	0.17	33.42	1.03	0.30	0.28	45.45
K_2O	0.80	0.16	1.12	0.66	1.01	1.13
SO_3	0.31	0.04	0.85	0.73	3.44	1.09
P_2O_5	0.14	n.d.	n.d.	2.55	0.28	<0.01
Mn_2O_3	n.d.	n.d.	n.d.	0.10	0.03	<0.01
LOI[a]	0.82	6.89	1.95	0.50	2.72	2.00–5.95[b]
Density (g/cm^3)[c]	2.25	2.52	2.37	2.94	3.12	2.17

[a] Loss on ignition at 1000 °C according to DIN EN 196-2.
[b] Loss on drying (LOD) at 105 °C (drying until $\Delta m < 0.01$ wt% within 24 h).
[c] Apparent density determined by helium pycnometry according to DIN 66137-2.

Mixing of the fresh mortars was conducted either in a RILEM mortar mixer for small batches (workability, setting time) or in a 30-dm^3 rotating pan mixer for bigger batches (mechanical strength, air permeability, XRD, 2D Micro-XRF, optical microscopy). Mixing of the pastes for the isothermal calorimetry was conducted using a lab stirrer at a rotation speed of 500 min^{-1}.

After mixing, the fresh mortars were cast into molds, and the uncovered molds were transferred to a climate chamber with either 23 °C/50% r.H. or 40 °C/35% r.H. for curing. After demolding at an age of 2–7 days, the specimens were further cured at the same conditions.

3. Methods

3.1. Physical and mechanical properties

The workability of the fresh mortars was studied by the determination of the spread flows with the Haegermann cone (d_1 = 70 mm, d_2 = 100 mm, h = 60 mm) and a jolting table, as described in DIN EN 1015-3:2007 [23] and with a bigger cone (d_1 = 30 mm, d_2 = 200 mm; h = 200 mm) in accordance with DIN EN 12350-5:2000 [24]. One OP AAM mortar was covered afterwards and additionally measured 24 h after the addition of water.

Additional experiments on the rheology of the fresh mortars were performed on specific mixes using a *ConTec Rheometer 4SCC*. The shear stress was measured indirectly as an electric current and will be reported as mA below. Initially, the fresh mortars were rotated at a speed of 0.5 min^{-1} for 10 s. Subsequently, the rotation speed was decreased to 0.05 min^{-1} using a sampling rate of 0.25 s. While every step was held constant for 5 s only the values of the last second of each step were taken for the evaluation to exclude errors from the change of the shear rate.

The determination of the setting times of the mortars was done by the Vicat test after DIN EN 196-3:2009 [25] with slight adjustments. The measurements were conducted on an automatic *Vicat Needle Instrument Model 7320/7312* using a needle with a mass of 300 g. To prevent leaching of the aggregates the measurements were conducted in dry environment (23 °C/50% r. H.).

The testing of the mechanical strength was performed using a *Toni-PRAX* testing machine for combined compressive strength and flexural strength testing. Specimen dimensions for strength testing were 40 mm × 40 mm × 160 mm. When samples were stored at elevated temperatures, they were allowed to cool down naturally before testing.

Table 2
Mix designs of the mortars.

	SF	SA	FA	CEM III/B	SS sln	NaOH sln.	Water	Salt
	mass fraction (kg/m^3)							
M2	–	–	324.4	324.4	–	–	264.1	1060.4
O1[a]	428.4	188.4	–	–	–	–	308.5	925.2
O2	300.3	132.1	–	–	–	–	216.2	1297.3
O3	327.6	144.1	–	–	–	–	188.6	1320.7
F1	–	–	597.6	–	220.8	84.5	23.1	1117.2

[a] Substitution of 11.2 kg/m^3 SA with Na_2CO_3 for the air permeability testing and XRD analysis; samples labeled O1_n.

Isothermal calorimetry of the pastes with compositions identical to the paste fractions of the corresponding mortars was performed in accordance with DIN EN 196-11:2018 [26] using a *TAM Air* calorimeter. The time between the addition of liquids and the start of the measurements was recorded and the obtained calorimetry data adjusted accordingly. The heat release during the first 30 min after the addition of the liquids was excluded for the calculation of the numerical value of the cumulative heat of reaction to minimize the influence of heat due to external mixing [27]. A CEM I 42.5 N paste (OPC paste) was prepared at a *w/b* of 0.40 by mass and used as an additional reference. All measurements were conducted in duplicate on samples with a mass of ~15 g. As the repeatability of the results was very good, only one calorimetry curve per paste is presented.

The determination of the gas permeability of the mortars was conducted in accordance with RILEM TC 116-PCD [28], but air was used as test gas and the specimen size was reduced (cylinders, $d = 50$ mm, $h = 50$ mm). Specimens were obtained by dry drill-cutting of cylinders from 300 mm × 300 mm × 100 mm specimens. Before the measurements, the specimens were dried at 40 °C in an oven until a constant mass ($\Delta m <$ 0.01 wt% within 24 h) was observed; this required usually 60–70 days.

3.2. Microstructural analyses

Samples for X-ray diffraction (XRD) were prepared by manual grinding; the obtained powders were filled into the sample holders by front loading. X-ray diffractograms were recorded on a *Rigaku Ultima IV* diffractometer in Bragg-Brentano geometry under the following experimental conditions: Cu Kα radiation ($\lambda = 1.5419$ Å), divergence slits of 10 mm (axial) and 0.5° (in plane), a sampling interval of 0.02° 2θ, a scanning speed of 0.5° 2θ min^{-1}, using a strip detector (*D/teX Ultra*).

2D-Micro-XRF was carried out using an *M4 Tornado* spectrometer with a Rh X-Ray tube ($U = 50$ kV, $I = 250$ µA), polycapillary X-ray optics and two silicon drift detector technology (*XFlash 430* detector) at 5 mbar and 20 °C. The spot size for the element mapping of the specimen surface (100 mm × 50 mm) was set to 20 µm.

Optical microscopy was conducted using an *Olympus SZX 16* stereo microscope with integrated ultraviolet (UV) mode. Samples were embedded in epoxy (*Conpox Resin BY 158; Conpox Hardener HY 2996*). Additionally, an UV-active pigment (*EPODYE*) was added to the epoxy, for better visibility of defects and other microstructural features. The epoxy was soaked into the samples under vacuum, and the subsequent hardening was conducted under a pressure of 15 bar.

4. Results

4.1. Fresh mortar properties

Fig. 1 shows the slump flows and spread flows of the fresh mortars. The different measurements correlated well, *i.e.* they yielded the same relative performance for the mortars. Thus, the results can be discussed based on the spread flows determined according to DIN EN 1015–3.

Mortar O1 had a spread flow of 221 mm, which was 80% of the spread flow of M2, while O2 and O3 exhibited considerably lower spread flows (63% and 48% compared to M2, respectively). The highest slump flow

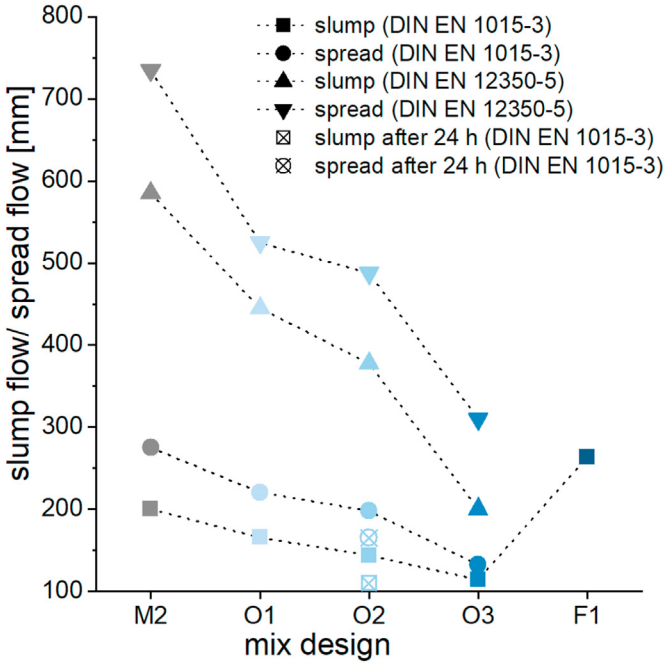

Fig. 1. Slump flows and spread flows of the fresh mortars determined in accordance with DIN EN 1015–3 and DIN EN 12350–5. Dotted lines serve as guide to the eye.

(264 mm) was determined for F1, which was 32% greater than of M2. 24 h after the addition of water the spread flow of O2 decreased to 165 mm, *i.e.* 95 % of the initial value.

Additional rheometer tests were carried out for mortars O1 and M2 (Fig. 2). Initially, O1 had a much higher yield stress (1405 mA) than M2 (106 mA). The shape of the shear stress-*versus*-shear rate curve of O1 indicated an approximately Bingham-like behavior, with the viscosity of O1 being higher than that of M2. One hour after the addition of water, the yield stress of both O1 (485 mA) and M2 (485 mA) was equal, while for both materials the viscosity was increased.

The shortest setting time of approximately 30 h was determined for mortar M2 (Fig. 3). The setting times of the OP AAM formulations O3 (~48 h), O2 (~72 h) and O1 (~192 h) were considerably longer. This behavior of the OP AAM mortars is in line with the still plastic behavior of O2 after 24 h (Fig. 1).

Fig. 4 shows the results of the isothermal calorimetry. After 7 days, the OPC paste had released a cumulative heat of 318 J/g (Fig. 4, right panel). The M2 paste released 125 J/g during the first 7 days and 201 J/g until 28 days after the addition of water. The heat released by O3 after 7 days (48 J/g) and 20 days (81 J/g) was slightly higher than for the O1/O2 paste (36 J/g after 7 days and 70 J/g after 20 days), but lower than for the F1 paste (55 J/g after 7 days and 102 J/g after 20 days). At 28 days, the cumulative heat of reaction had increased to 91 J/g for O1/O2, which was 45% of the heat released by M2 at the same age.

The heat flow curve of the OPC paste (Fig. 4, left panel) exhibited a

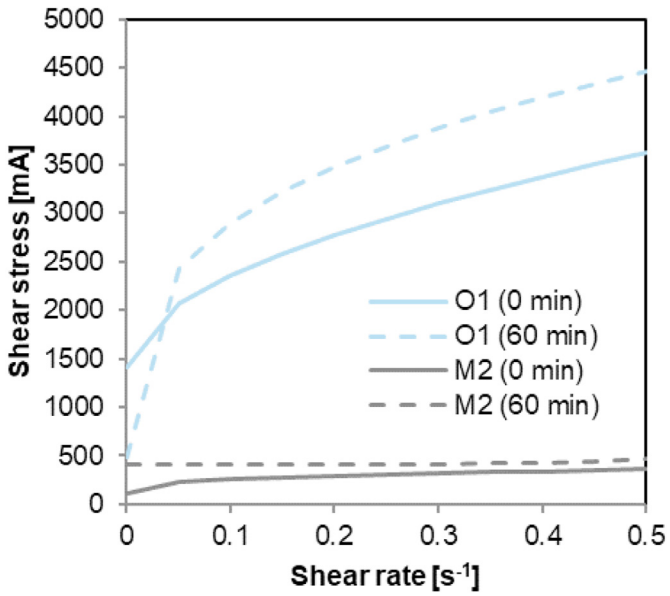

Fig. 2. Results of the rheometer measurements for mortars O1 and M2 immediately after the addition of water (0 min) and 1 h after the addition of water (60 min).

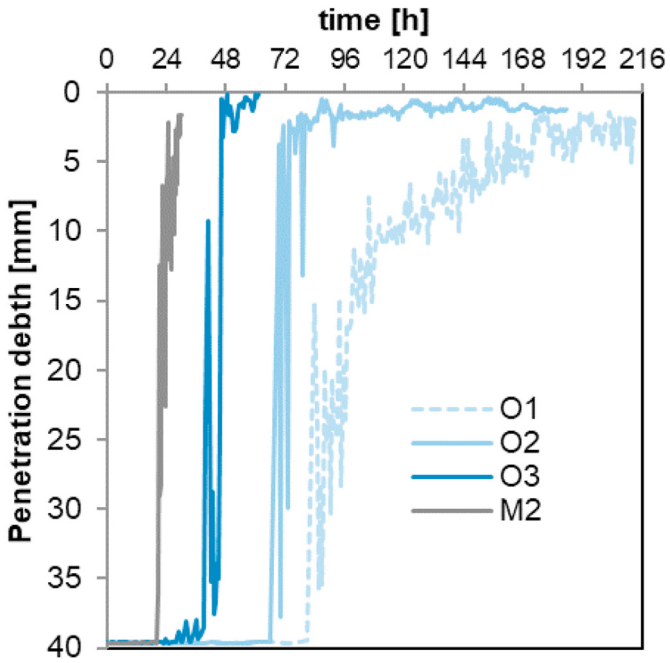

Fig. 3. Penetration depths of the mortars at 23 °C determined with an automatic Vicat device.

main hydration peak at ~11 h, a shoulder at ~13.5 h and a second shoulder at ~40 h. In the heat flow curve of M2, a peak with a comparable shape, but lower intensity, as the main peak of the OPC paste was detected at later ages (~32 h), followed by a weak second peak after ~47 h. No distinct peak could be identified for the AAM pastes besides the initial dissolution peak after the addition of the liquids. After this peak, the heat flow dropped below 0.2 mW/g and remained at this low level (Fig. 4, right panel).

4.2. Mechanical and physical properties of the hardened mortars

The reference mortar M2 achieved a compressive strength of 25.7 MPa after 28 days of curing at 23 °C/50% r.H.; a significant further increase to 30.9 MPa occurred up to 91 days (Fig. 5, right panel). A quite comparable behavior was observed for F1 with slightly higher absolute values (27.4 MPa at 28 days and 36.2 MPa at 91 days). The strength of the OP AAM mortars increased more continuously over the time. The early compressive strength of the OP AAM mortars was only 15–45% of M2 after 28 days, whereas the relative strength after 91 days was 55% for O1 (16.9 MPa), 40% for O2 (12.2 MPa) and 91% for O3 (28.2 MPa). After 91 days O3 had the highest flexural strength of all AAM mortars (6.7 MPa; 92% of M2).

Storage at 40 °C/35% r.H. led to a considerably accelerated strength development (Fig. 5). After 28 days, mortar O2 had achieved the compressive strength of the 23 °C-cured mortar M2, and the compressive strength of O3 was approximately equal to the final strength of F1, cured at the lower temperature. Afterwards, no further increase of the compressive strength was observed (Fig. 5, right panel). The flexural strength of O3 showed a decrease after 28 days and that of O2 after 56 days. Mortar F1 reached the highest compressive strength (47.3 MPa) and flexural strength (6.8 MPa) after 91 days.

M2 exhibited an air permeability on the order of 10^{-18} m^2 (Table 3) after hardening at 23 °C/50% r.H. Thus, the workability (Fig. 1), the compressive strength (Fig. 5, right panel) and the air permeability (Table 3) are in very good agreement with previously published data for this material [2,10]. The air permeabilities of the AAM mortars were about two orders (O2: 5×10^{-17} m^2 and O3: 9×10^{-17} m^2) to three orders (O1, F1: ~10^{-15} m^2) of magnitude higher than the permeability of M2. An increased curing temperature (40 °C/35% r.H.) had no significant influence on the permeability of O1, whereas it led to an increase for O2 and O3 to approximately 10^{-15} m^2, and a decrease of the permeability of F1 to approximately 10^{-16} m^2 (Table 3).

4.3. Structure of the hardened mortars

Fig. 6 shows the XRD patterns of the mortars after 91 days of storage. The rock salt phases halite (NaCl; PDF # 00-005-0628), mirabilite ($Na_2SO_4 \cdot 10H_2O$; PDF # 00-011-0647), arcanite (K_2SO_4; PDF # 00-025-0681) and anhydrite ($CaSO_4$; PDF # 00-037-1496) were identified in the cured mortars (Fig. 6, left panel). Thus, they had remained at least partly stable in the OP AAM mortars, while anhydrite was fully consumed in M2 and F1. Curing at 40 °C (Fig. 6, right panel) caused the virtually complete consumption of mirabilite in all mortars.

In mortar M2, the AFm phase Friedels' salt (PDF # 01-089-8294) had formed; in addition, amorphous phase (presumably calcium aluminum silicate hydrates; C(-A)-S-H) and calcite (due to carbonation) were identified. The OP AAM formulations exhibited signs of carbonation as well (thermonatrite; PDF # 00-008-0448), but only at the lower curing temperature (Fig. 6). The natrite in the O1_n sample is a residue from its addition to the starting mix to minimize the aluminum excess (Table 2). The preconditioning of the SA (sieving and Na_2CO_3 addition; see Section 2) did not fully prevent the formation of aluminum hydroxide (gibbsite; PDF # 00-033-0018) in the OP AAM (Fig. 6). A broadening of the amorphous hump towards higher diffraction angles indicated the formation of sodium aluminosilicate gel (N-A-S-H) in the AAM mortars. In addition, O1 contained minor amounts of faujasite-type zeolites (PDF # 00-012-0246) and EMT-type zeolites (PDF # 00-012-0246), apparently with a higher abundance when the mortars were stored at 40 °C/35% r.H. (Fig. 6). In the F1 mortar, mullite and quartz are residues from the employed FA. No crystalline reaction products were identified in this mortar for both curing temperatures.

The Micro-XRF measurements of O3 (Fig. 7) revealed alumina-rich nodules or agglomerations with a range of sizes in the OP AAM mortars. Larger alumina agglomerations are preferably located at the surface of the Si- and Al-free grains – *i.e.* the rock salt aggregate particles. While smaller alumina centers tended to occur at a higher number in O3 (Fig. 7, right panel), the bigger agglomerates tended to be more numerous in O2 (Fig. 7, left panel).

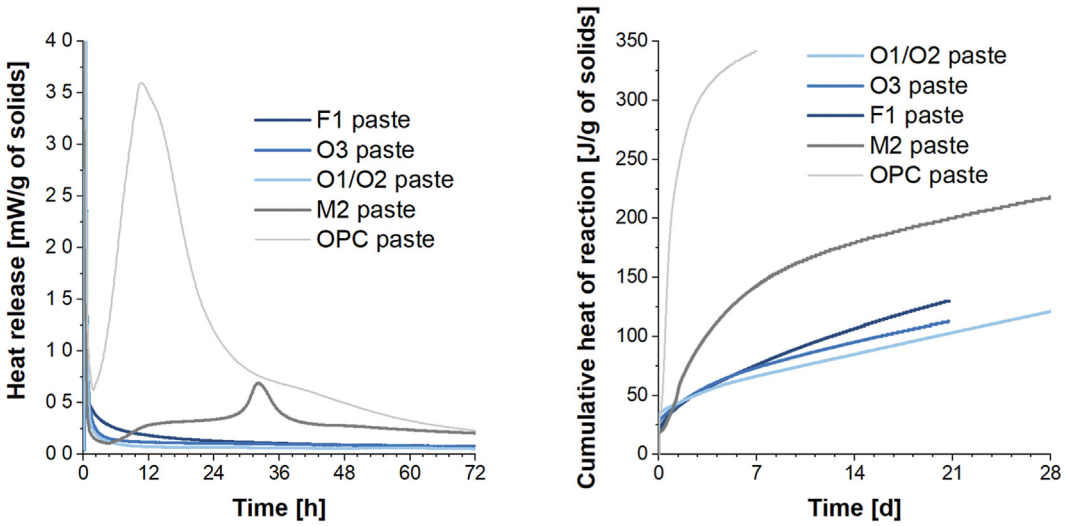

Fig. 4. Heat release rate (left) and cumulative heat release (right) of pastes O1/O2, O3, F1, M2 and an OPC paste.

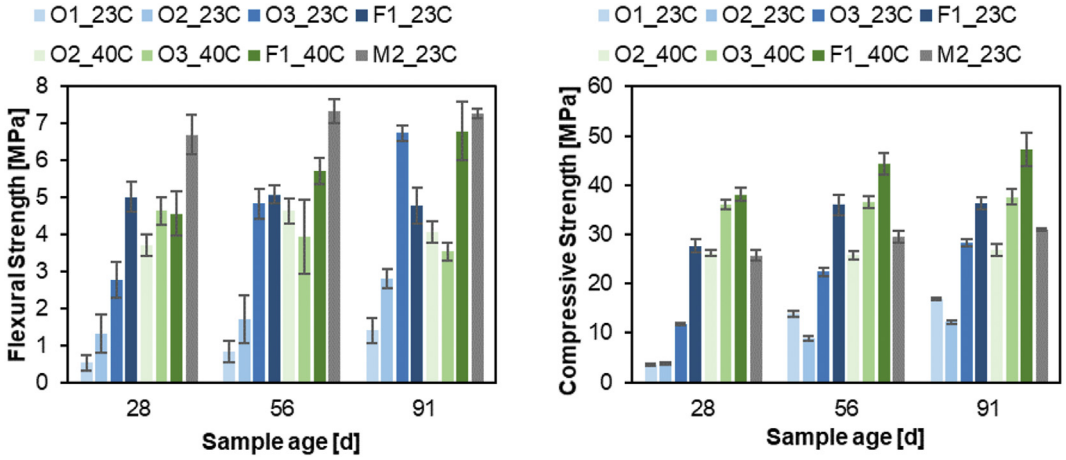

Fig. 5. Development of the flexural strength (left) and compressive strength (right) of the mortars as measured over a time of 91 days at 23 °C/50% r.H. or 40 °C/35% r.H., respectively. The error bars represent one standard deviation in each direction.

Table 3
Air permeability of the mortars after 91 days of storage at 23 °C/50% r.H. or 40 °C/35% r.H., and subsequent drying at 40 °C until constant mass (*K*: air permeability, mean of 3 specimens; SD: standard deviation).

Sample Name	K (m^2)	SD (m^2)
O1_23C	2.1×10^{-15}	2.5×10^{-15}
O2_23C	4.7×10^{-17}	4.3×10^{-17}
O3_23C	8.7×10^{-17}	2.2×10^{-17}
F1_23C	1.3×10^{-15}	1.5×10^{-15}
M2_23C	1.1×10^{-18}	4.1×10^{-19}
O1_40C	1.9×10^{-15}	1.3×10^{-15}
O2_40C	1.2×10^{-15}	6.6×10^{-16}
O3_40C	1.6×10^{-15}	4.5×10^{-16}
F1_40C	2.6×10^{-16}	3.9×10^{-17}

Fig. 8 (top left panel) shows that mortar O1 after storing under normal conditions (23 °C/50% r.H.) included a considerable amount of air voids. Few thin lines of lighter color indicate minor microcrack formation. Comparison with the micrographs of the other mortars indicates that O1 had a somewhat increased amount of microcracks compared to the other 23 °C-cured material. O2 shows major spots of very light color, indicating the loosely agglomerated alumina (gibbsite) as shown in Figs. 6–8 (middle).

After storage at 40 °C/35% r.H., the amount of air voids was reduced in all OP AAM mortars compared to the lower curing temperature, but a more pronounced drying effect was found, as indicated by an increased number of microcracks for all mortars (Fig. 8). For O3, this more pronounced microcrack formation is assumed to be a main reason for the decreased flexural strength compared to the 23 °C-cured material (Fig. 5).

5. Discussion

The workability of the OP AAM mortars was inferior to that of mortar M2, while mortar F1 was more flowable than M2 (Fig. 1). The nominal volume-based *l/s* of F1 was 0.89, which is lower than the *w/b* of the OP AAM mortars (1.07–1.16) but comparable to the *w/b* of M2 (0.93). Thus, it is likely that the most important reason for the better workability of mortar F1 was the larger particle size, and thus lower specific surface area, of the fly ash, compared to the SF in the OP AAM mortars.

For mortar F1, the main peak of the heat flow curves is related to this release of ions to the activator solution [16,17]. A second peak after the dormant period, which would be expected to signify the poly-condensation of the N-A-S-H gel network [16,17], could not be identified in the present study. The reason is presumably the high apparent activation energy for the dissolution of the FA in NaOH- and SS-activated

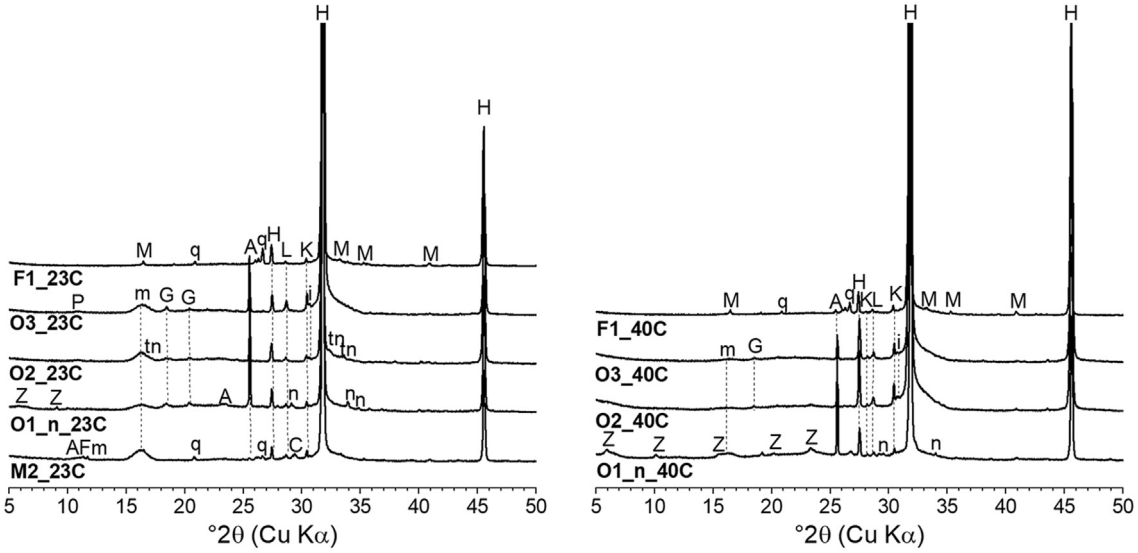

Fig. 6. Diffraction patterns of the mortars after storage at 23 °C/50% r.H. (left) or 40 °C/35% r.H. (right) for 91 days. *M* = mullite, *q* = quartz, *A* = anhydrite, *H* = halite, *L* = langbeinite, *K* = arcanite, *m* = mirabilite, *G* = gibbsite, *n* = natrite, *tn* = thermonatrite, *C* = calcite, *Z* = zeolite, *AFm* = Friedels' salt.

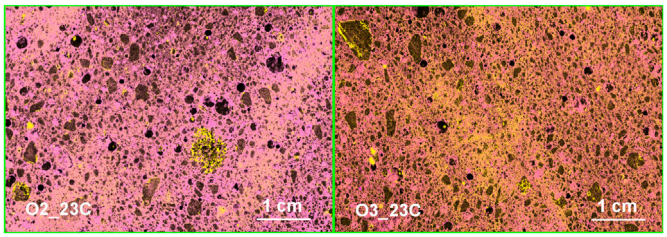

Fig. 7. XRF maps of mortars O2 (left) and O3 (right) after 91 days storage at 23 °C/50% r.H. Pink color refers to silicon and yellow color refers to aluminum. (For interpretation of the references to color in this figure legend, the reader is referred to the Web version of this article.)

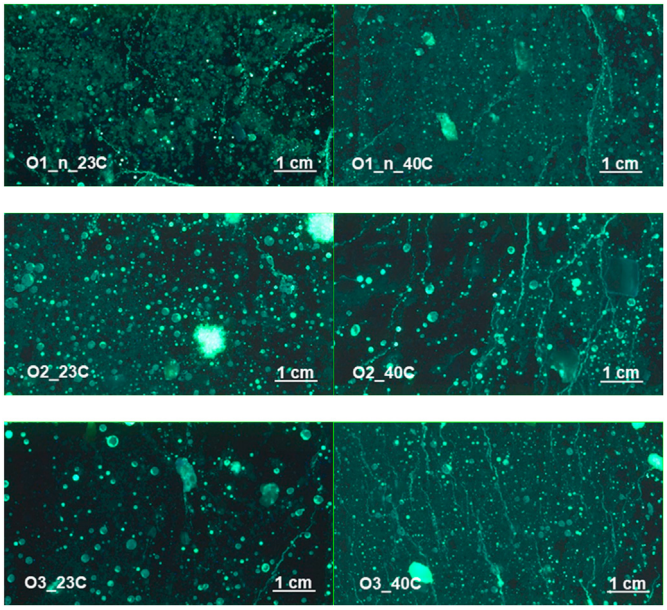

Fig. 8. Optical microscopy under UV light of the mortars O1_n (top), O2 (middle), O3 (bottom) after 91 days of storage at 23 °C/50% r.H. (left column) and after storage at 40 °C/35% r.H. (right column).

AAFA at room temperature [16,17,29]. For the OP AAMs of this study, a similar behavior was observed, *viz.* a high heat flow only during the beginning of the reactions. In addition, a comparable activation energy as for AAFAs was reported for the dissolution of silica fume and silica aerogel in NaOH-solution [30,31]. Curing at elevated temperature overcomes this activation barrier. For example, the dissolution rate of NaOH-activated FA is doubled by increasing the temperature from 20 °C to 30 °C [16,17,29], which explains the increased early strength of the samples which have been stored at 40 °C in the present study, compared to the 23 °C-cured mortars (Fig. 5) The SF reacts only partly and thus limits the formation of the strength forming N-A-S-H gel in the OP AAM mortars [15].

An important difference between the present work and previous studies of OP AAM binders with analogous compositions [15,21] was the absence, or very limited occurrence, of crystalline zeolites as reaction products (Fig. 6). The low amounts of faujasite-type zeolites (Si/Al ratio ~2.3 mol/mol) and EMT-type (3.4 mol/mol) zeolites in mortar O3 may indicate that the precipitated N-A-S-H gel had a Si/Al ratio significantly higher than 1, again in contrast the earlier studies, in which the OP AAMs were cured at elevated temperatures [15,21]. This would be in line with the general observations that a low reacted silicon content, an increased curing temperature and a high water content favor zeolite formation in AAMs [32,33].

The air permeabilities of the AAM mortars (10^{-15}–10^{-17} m^2; Table 3) were in accord with the range of published permeabilities of FA-based AAMs [34–36]. The lowest air permeability was found for mortar O2, which was, however, still one to two orders of magnitude higher than the permeability of the reference mortar M2. However, compared to other conventional cement-based materials, the permeability of mortars O2 and O3 can still be considered low and presumably sufficient for the intended application. Nevertheless, microcrack formation due to drying shrinkage, especially at 40 °C/35% r.H. (Fig. 8), and considerable gibbsite precipitation in nodules (Figs. 6–8), are potential problems which, therefore, require further studies.

6. Conclusions

The results of this study suggest that AAMs can be promising alternative binders for the production of salt mortars, mainly because of the much lower heat of reaction and extended setting times, both of which are considered to be beneficial regarding the development of early stresses and cracks in concrete sealing structures for nuclear waste

repositories. In particular, no distinct peaks occurred during calorimetry for the AAMs after the initial wetting and dissolution, due to the slow subsequent dissolution at moderate temperatures. This behavior is well-known for AAFA, but has been demonstrated for OP AAMs in this study for the first time.

After 28 days, the cumulative heat of reaction of the O1/O2 paste was only 45% of the heat released by M2, a blended cement currently considered for concrete sealing structures in evaporite rock. This indicates that the temperature increase that would occur under sealed conditions, as those encountered during construction of sealing structures, is considerably lower than for M2. These slow reaction kinetics cause relatively low early mechanical strength compared to the reference (M2). However, with increasing sample age, the differences decrease, and specific mixes reach equal (O3) or even higher (F1) strength than the reference after 91 days. The formation of crystalline tectosilicates in the OP AAMs, which is common for this type of AAMs, can be decreased (40 °C) or virtually avoided (23 °C) by limiting the curing temperature.

Nevertheless, optimization of the AAM formulations is required regarding workability (OP AAMs) and air permeability (OP AAMs and AAFA). The differences in workability between the AAMs are strongly related to the particle sizes of the solids in the pastes, leading to an increased water demand of the OP AAM mortars. The higher mechanical strength of F1 compared to the OP AAM mortars is presumably caused by the formation of a higher amount of N-A-S-H gel with a higher Si/Al-ratio gel in the former. The air permeability of the AAM mortars was higher than that of reference M2, but still comparatively low, especially for mix O2. Curing at 40 °C/35% r. H. led to an increased early strength, but also to the formation of more microcracks due to drying shrinkage, compared to curing at 23 °C/50% r. H.

Taken together, the present results show that AAMs can provide benefits for the construction of sealing structures in evaporite rock in terms of heat evolution, but further developments are required as regards workability in the fresh state and permeability in the hardened state. Further studies are also required to determine the chemical durability of AAMs in the relevant environments, i.e. saline solutions.

Declaration of competing interest

The authors declare that they have no known competing financial interests or personal relationships that could have appeared to influence the work reported in this paper.

Acknowledgement

The authors acknowledge financial support from the *Bundesanstalt für Materialforschung und -prüfung* (*BAM*) within the research project "Seal-WasteSafe".The authors thank the *Bundesgesellschaft für Endlagerung* (*BGE*) and the Kaliwerk Zielitz of the *K+S KALI GmbH* for the supply of the rock salt aggregates.

References

[1] W. Brewitz, T. Rothfuchs, Concepts and technologies for radioactive waste disposal in rock salt, Acta Montan. Slovaca 12 (2007) 67–74.
[2] Deutsche Gesellschaft zum Bau und Betrieb von Endlagern für Abfallstoffe mbH (DBE), Verfüllmaterial für Strecken mit hohen Anforderungen Materialeigenschaften und Materialkennwerte Salzbeton M2, Bundesamt für Strahlenschutz, Salzgitter, 2004.
[3] Gesellschaft für Anlagen- und Reaktorsicherheit (GRS) gGmbH, Vorläufige Sicherheitsanalyse für den Standort Gorleben, AP 9.2, Integrität Geotechnischer Barrieren, Teil 2, Vertiefte Nachweisführung. GRS, Braunschweig, 2012.
[4] Gesellschaft für Anlagen- und Reaktorsicherheit (GRS) gGmbH, Vorläufige Sicherheitsanalyse für den Standort Gorleben, AP 9.2, Integrität Geotechnischer Barrieren. Teil 1, Vorbemessung. GRS, Braunschweig, 2012.
[5] T. Runčevski, R.E. Dinnebier, D. Freyer, Dehydration of the Sorel cement phase $3Mg(OH)_2{\cdot}MgCl_2{\cdot}8H_2O$ studied by in situ synchrotron X-ray powder diffraction and thermal analyses, Z. Anorg. Allg. Chem. 640 (2014) 100–105, https://doi.org/10.1002/zaac.201300229.
[6] J. Stahlmann, C. Missal, A. Gährken, Interaction between salt concrete sealing structures and rock salt, in: L. Roberts, K. Mellegard, F. Hansen (Eds.), Mechanical Behavior of Salt VIII, Taylor & Francis, London, 2015, pp. 153–158.
[7] S.A. Walling, J.L. Provis, Magnesia-based cements: a journey of 150 Years, and cements for the future? Chem. Rev. 116 (2016) 4170–4204, https://doi.org/10.1021/acs.chemrev.5b00463.
[8] C. Cau Dit Coumes, S. Courtois, D. Nectoux, S. Leclercq, X. Bourbon, Formulating a low-alkalinity, high-resistance and low-heat concrete for radioactive waste repositories, Cem. Concr. Res. 36 (2006) 2152–2163, https://doi.org/10.1016/j.cemconres.2006.10.005.
[9] J.L. García Calvo, A. Hidalgo, C. Alonso, L. Fernández Luco, Development of low-pH cementitious materials for HLRW repositories Resistance against ground waters aggression, Cem. Concr. Res. 40 (2010) 1290–1297, https://doi.org/10.1016/j.cemconres.2009.11.008.
[10] B. Lothenbach, G. Le Saout, M. Ben Haha, R. Figi, E. Wieland, Hydration of a low-alkali CEM III/B–SiO_2 cement (LAC), Cem. Concr. Res. 42 (2012) 410–423, https://doi.org/10.1016/j.cemconres.2011.11.008.
[11] K. Jantschik, O. Czaikowski, U. Hertes, T. Meyer, H.C. Moog, B. Zehle, Development of Chemical-Hydraulic Models for the Prediction of Long-Term Sealing Capacity of Concrete- Based Sealing Materials in Rock Salt, 2018.
[12] N.S. Awwad, A.A.M. Daifullah, Preconcentration of U(VI) from aqueous solutions after sorption using Sorel's cement in dynamic mode, J. Radioanal. Nucl. Chem. 264 (2005) 623–628, https://doi.org/10.1007/s10967-005-0762-1.
[13] K. Schollbach, Synthese und Charakterisierung von Oxysalz-Zementen und ihren Phasen, Dissertation, Martin-Luther-Universität Halle-Wittenberg, 2015.
[14] J.L. Provis, J.S.J. van Deventer, Alkali Activated Materials: State-Of-The-Art Report, RILEM TC 224-AAM, Springer, Dordrecht, 2014.
[15] P. Sturm, S. Greiser, G.J.G. Gluth, C. Jäger, H.J.H. Brouwers, Degree of reaction and phase content of silica-based one-part geopolymers investigated using chemical and NMR spectroscopic methods, J. Mater. Sci. 50 (2015) 6768–6778, https://doi.org/10.1007/s10853-015-9232-5.
[16] Z. Hu, M. Wyrzykowski, P. Lura, Estimation of reaction kinetics of geopolymers at early ages, Cem. Concr. Res. 129 (2020), 105971, https://doi.org/10.1016/j.cemconres.2020.105971.
[17] Z. Sun, A. Vollpracht, Isothermal calorimetry and in-situ XRD study of the NaOH activated fly ash, metakaolin and slag, Cem. Concr. Res. 103 (2018) 110–122, https://doi.org/10.1016/j.cemconres.2017.10.004.
[18] A. Castel, S.J. Foster, T. Ng, J.G. Sanjayan, R.I. Gilbert, Creep and drying shrinkage of a blended slag and low calcium fly ash geopolymer concrete, Mater. Struct. 49 (2016) 1619–1628, https://doi.org/10.1617/s11527-015-0599-1.
[19] Y. Ma, G. Ye, The shrinkage of alkali activated fly ash, Cem. Concr. Res. 68 (2015) 75–82, https://doi.org/10.1016/j.cemconres.2014.10.024.
[20] P. Sturm, G.J.G. Gluth, H.J.H. Brouwers, H.-C. Kühne, Shrinkage and bond behaviour of one-part alkali-activated mortars, in: A. Barčević, M.J. Rukavina, D. Damjanović, M. Guadagnini (Eds.), Proceedings of the International Conference on Sustainable Materials, Systems and Structures – Vol. 3: Durability, Monitoring and Repair of Structures, Rovinj, Croatia, RILEM Publications, Paris, 2019, pp. 103–110.
[21] P. Sturm, G.J.G. Gluth, S. Simon, H.J.H. Brouwers, H.-C. Kühne, The effect of heat treatment on the mechanical and structural properties of one-part geopolymer-zeolite composites, Thermochim. Acta 635 (2016) 41–58, https://doi.org/10.1016/j.tca.2016.04.015.
[22] P. Sturm, H.-C. Kühne, G.J.G. Gluth, Salzmörtel und Salzbetone auf der Basis von Geopolymeren, vol. 7, German patent application Nr, 2019, 102019114416.
[23] Deutsches Institut für Normung (DIN), DIN EN 1015-3 Methods of Test for Mortar for Masonry – Part 3: Determination of Consistence of Fresh Mortar (By Flow Table), Beuth Verlag, Berlin, 2007.
[24] Deutsches Institut für Normung (DIN), DIN EN 12350-5 Prüfung von Frischbeton – Teil 5: Ausbreitmaß, Beuth Verlag, Berlin, 2000.
[25] Deutsches Institut für Normung (DIN), DIN EN 196-3 Prüfverfahren für Zement – Teil 3: Bestimmung der Erstarrungszeiten und der Raumbeständigkeit, Beuth Verlag, Berlin, 2009.
[26] Deutsches Institut für Normung (DIN), DIN EN 196-11 Prüfverfahren für Zement – Teil 11: Hydratationswärme – Isotherme Wärmeflusskalorimetrie-Verfahren, Beuth Verlag, Berlin, 2019.
[27] L. Wadsö, F. Winnefeld, K. Riding, P. Sandberg, Calorimetry, in: K. Scrivener, R. Snellings, B. Lothenbach (Eds.), A Practical Guide to Microstructural Analysis of Cementitious Materials, CRC Press, Boca Raton, 2016, pp. 37–74.
[28] RILEM TC 116-PCD, Tests for gas permeability of concrete, Mater. Struct. 32 (1999) 174–179.
[29] F. Škvára, L. Kopecký, V. Šmilauer, Z. Bittnar, Material and structural characterization of alkali activated low-calcium brown coal fly ash, J. Hazard. Mater. 168 (2009) 711–720, https://doi.org/10.1016/j.jhazmat.2009.02.089.
[30] A.G. Okunev, S.A. Shaurman, A.F. Danilyuk, Y.I. Aristov, G. Bergeret, A. Renouprez, Kinetics of the SiO_2 aerogel dissolution in aqueous NaOH solutions: experiment and model, J. Non-Cryst. Solids 260 (1999) 21–30, https://doi.org/10.1016/S0022-3093(99)00568-2.
[31] Y. Zhong, X. Qiu, J. Gao, Z. Guo, Chemical structure of Si–O in silica fume from ferrosilicon production and its reactivity in alkali dissolution, ISIJ Int. 59 (2019) 1098–1104, https://doi.org/10.2355/isijinternational.ISIJINT-2018-516.
[32] P. Duxson, J.L. Provis, G.C. Lukey, S.W. Mallicoat, W.M. Kriven, J.S.J. van Deventer, Understanding the relationship between geopolymer composition, microstructure and mechanical properties, Colloids Surf. A 269 (2005) 47–58, https://doi.org/10.1016/j.colsurfa.2005.06.060.

[33] J.L. Provis, G.C. Lukey, J.S.J. van Deventer, Do geopolymers actually contain nanocrystalline zeolites? A reexamination of existing results, Chem. Mater. 17 (2005) 3075–3085, https://doi.org/10.1021/cm050230i.
[34] G.J.G. Gluth, W.D.A. Rickard, Design and characterization of fly ash-based geopolymer concretes for a round-robin durability testing program, in: C. Leonelli, M. Romagnoli (Eds.), Geopolymers: the Route to Eliminate Waste and Emissions in Ceramic and Cement Manufacturing, Società Ceramica Italiana, Bologna, 2015, pp. 67–70.
[35] W.D.A. Rickard, G.J.G. Gluth, K. Pistol, In-situ thermo-mechanical testing of fly ash geopolymer concretes made with quartz and expanded clay aggregates, Cem. Concr. Res. 80 (2016) 33–43, https://doi.org/10.1016/j.cemconres.2015.11.006.
[36] K. Sagoe-Crentsil, A. Taylor, T. Brown, Transport properties of geopolymer systems and their effect on binder permeability and durability, in: 13th International Congress on the Chemistry of Cement, 2011. Madrid, Spain.